Computer Modeling in
Engineering & Sciences

Tech Science Press

Doi:10.32604/cmes.2025.064773

ARTICLE

Calculation for Arc Transition Moment of Sliding Electric Contact Pair Based on Coupled FE-BE Simulation

Xiangyu Du, Xiaoquan Lu, Tianyou Zheng, Shaowei Liu* **and Bo Cao**

Air Defence and Antimissile School, Air Force Engineering University, Xi'an, 710051, China

*Corresponding Author: Shaowei Liu. Email: lsw3721@163.com

Received: 23 February 2025; Accepted: 29 May 2025; Published: 30 June 2025

ABSTRACT: Sliding electrical contact is a common phenomenon in electrical equipment and affects performance. In this paper, the mechanism of sliding electric contact pair transition and the moment when transition occurs are investigated using the railgun as an example. Transition is the phenomenon where the contact between the armature and rails changes from solid-solid contact to solid-arc-solid contact. In this paper, the finite element-boundary element coupling method (FE-BE method) is used to simulate the process of armature movement. Then, the force, thermal, and electrical parameters on the armature/rail contact surface are analyzed to explore the development of contact separation. Finally, the occurrence of the transition is judged based on the Townsend discharge model (improved by Rogowski). A Small-caliber railgun firing test was carried out to validate the methodology presented in this paper. Results show that the drop edge of the current will result in the armature/rail not being able to make full contact, and the contact gap may break down, leading to a sharp increase in contact resistance and deterioration of railgun performance. Judging the occurrence of transition based on the evolution of the contact gap and the Townsend discharge model is reliable. The research provides new ideas for studying railgun transition and sliding electric contact failure.

KEYWORDS: Sliding electric contact; electromagnetic railgun; transition; FE/BE method

1 Introduction

An electromagnetic railgun is a launching device that can instantaneously and efficiently convert high-power electric energy into kinetic energy, which has significant advantages such as high output power, high energy efficiency, short launching interval, and so on [1–3]. Thus, railguns have promising applications in areas such as launching kinetic energy weapons and firing plasma [4,5]. Armature and rails are the core components of a railgun, the two parts realize energy transfer through sliding electrical contact during the railgun operation. Due to the rapid movement of the armature and the high loads on the rails, it is very difficult to maintain stable contact between the armature and the rails. Transition is the process of changes from solid-solid contact to plasma contact between the armature and the rails, and also represents the various types of damage caused by this process [6–8]. The transition will cause arcs between the armature and the rails and cause the rails to be ablated.

Contact separation between the armature and the rails is the direct cause of the transition. Armature/rail gap (A/R Gap) occurs due to the effects of the negative electromagnetic force, armature melting, wear, and so on. Due to the potential difference between the armature and rails, when the A/R Gap is electrically broken down, additional arc resistance is added to the contact resistance of the railgun, deteriorating the railgun's performance [9].

A variety of factors may cause the contact between the armature and the rails to become unstable and produce transition: Wang et al. believed that when the contact pressure is less than the pressure specified in the "1g/A" law, the armature and rails are not enough to maintain contact, and the transition will occur [10]; Stefani et al. explored the effect of armature arm force reversal during the current drop and concluded that this phenomenon would lead to the transition [6]; Zhu et al. believed that armature wear and erosion is the direct cause of transition [11]; Dong cited uneven rail surfaces as the likely cause of railgun transition [12]; Gendel et al. investigated the effect of velocity skin effect (VSE) on transition under hypervelocity [13]; Machado studied the critical state of transition and obtained the velocity of the armature at the onset of transition [14]. Due to the drastic changes in the contact state and the complex working environment of railguns, the above studies could not provide a complete description of the influencing factors of transition. In particular, there has been no direct consideration of how the armature and rails are electrically broken down to cause plasma contact in previous research.

This paper analyzes the internal ballistic process of the railgun and the contact separation phenomenon in armature motion, puts forward a transition judgment model based on the electric breakdown condition, and numerically simulates the operation of the railgun by using the FE-BE method based on Ls-dyna. This research will help to understand the formation mechanism of the railgun transition.

2 Materials and Methods

2.1 Structure of the Railgun

The railgun used in this study consists of convex rails made of copper C18150 and an armature made of 7075 aluminum alloy material, the shells material made of steel and the insulator is made of a composite material of glass fibers and epoxy resin. The geometry structure and mesh model of the railgun are shown in Fig. 1. The armature and rails material parameters are shown in Table 1.

The railgun used in this study consists of convex rails made of copper C18150 and an armature made of 7075 aluminum alloy. The shell material is steel, and the insulator is made of a composite material of glass fibers and epoxy resin. The geometry structure and mesh model of the railgun are shown in Fig. 1. The armature and rail material parameters are shown in Table 1.

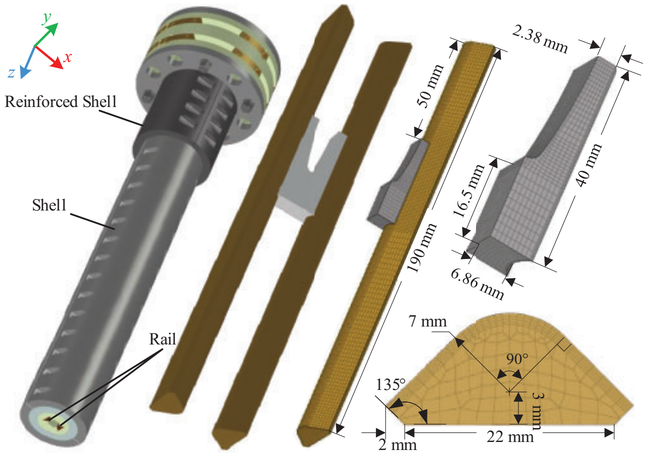

Figure 1: Geometry structure and mesh model of the railgun

Table 1: Material parameters

Property	Rail	Armature
Electrical resistivity [$10^{-2}(\Omega\cdot\text{mm}^2)/\text{m}$]	1.777	2.83
Temperature coefficient of resistivity [10^{-3} °C^{-1}]	3.81	4.07
Magnetic permeability	1	1
Melting point [°C]	1085	658
Density [kg/m^3]	8960	2710
Heat capacity [J/(kg·K)]	385	900
Thermal conductivity [(W·m)/K]	410	238
Thermal expansion coefficient [10^{-6} K^{-1}]	16.6	23
Young's modulus [Pa]	1.1×10^{11}	6.5×10^{10}
Poisson's ratio	0.35	0.33

The simulation is meshed using eight-node hexahedral cells with a total of 111,660 elements and 128,086 nodes and the maximum size of mesh is 0.5 mm. The armature and rails surface meshes are refined, as shown in Fig. 1.

In the model, the armature length is 40 mm (of which the armature arm length is 23.5 mm), the maximum interference is 0.18 mm, the initial position of the armature is 50 mm from the end of the rails, the rails spacing is 13.72 mm at the narrowest point, and the armature motion distance is 100 mm in the simulation. Specific structural parameters are also labeled in Fig. 1.

2.2 *Multi-Field Governing Equations*

The internal ballistic process of the railgun is affected by the coupled electric-magnetic-thermal-structural fields. In order to study the changes in the physical properties of the railgun, we analyze the coupling relationship between the multi-fields, as shown in Fig. 2.

For the electromagnetic field, since the frequency range of the pulsed power supply is in kHz (the frequency range of the railgun power supply can be obtained by joint time-frequency analysis), we neglect the displacement current and solve Maxwell's equations under the assumption of a magnetically quasi-static field. Using the A-φ-A format of Maxwell's equations and considering the Lorentz effect on current density, that is $\boldsymbol{J} = \sigma\left(\boldsymbol{E} + \boldsymbol{v} \times \boldsymbol{B}\right)$, we obtain the electromagnetic field governing equations:

$$\nabla^2 \boldsymbol{A} - \mu\sigma\left(\frac{\partial \boldsymbol{A}}{\partial t} + \nabla\phi\right) + \mu\sigma v \times \left(\nabla \times \boldsymbol{A}\right) = -\mu \boldsymbol{J}_s, \tag{1}$$

$$\nabla \cdot \left(-\sigma\frac{\partial \boldsymbol{A}}{\partial t} - \sigma\nabla\phi + \sigma v \times \left(\nabla \times \boldsymbol{A}\right)\right) = 0, \tag{2}$$

where $\boldsymbol{A}$ is the magnetic vector potential, φ is the electric scalar potential, μ and σ are the magnetic permeability and electric conductivity of the material, respectively, $\boldsymbol{J}_s$ is the source current density, and v is the velocity of conductor motion.

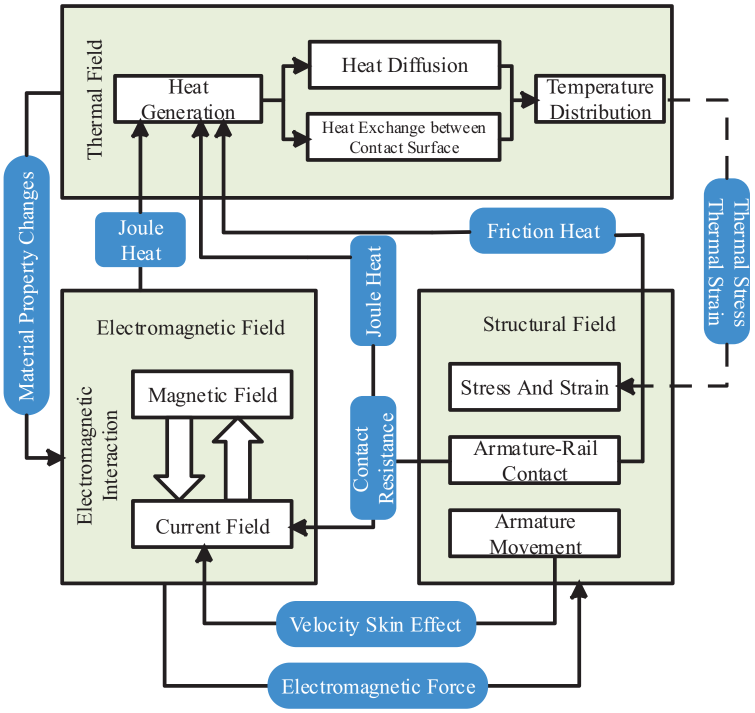

Figure 2: Multi-physics field coupling relations of railguns

The numerical calculation is less stable due to the presence of v. Therefore, Lagrange coordinates are used to describe the moving conductor, in which the velocity term v will be transformed from explicit to implicit. In turn, several key physical quantities that relate to the performance of the railgun can be derived:

$$\boldsymbol{J} = -\frac{1}{\mu_0}\nabla^2\boldsymbol{A}, \tag{3}$$

$$B_x = \frac{\partial \boldsymbol{A}}{\partial y}, B_y = -\frac{\partial \boldsymbol{A}}{\partial x}. \tag{4}$$

For the general operating environment of an electromagnetic railgun, it can be assumed that air does not conduct electricity. Therefore, the electromagnetic governing equations in the air region degenerate into Laplace's equations:

$$\nabla^2\boldsymbol{A} = 0. \tag{5}$$

Considering the force characteristics of the railguns and the fact that the materials of the railguns are all non-ferromagnetic, we use the Maxwell tensor method to solve the Lorentz force equation:

$$\boldsymbol{F}_{em} = \boldsymbol{J} \times \boldsymbol{B} = -\sigma\left(\frac{\partial \boldsymbol{A}}{\partial t} + \nabla\phi\right) \times (\nabla \times \boldsymbol{A}). \tag{6}$$

For the thermal field of the railgun, we use Fourier's law to describe the heat transfer phenomena in the railgun due to the short operating time of the railgun:

$$\rho c\left(\frac{\partial T}{\partial t}+v\nabla T\right)-\nabla\cdot(\kappa\nabla T)=Q, \tag{7}$$

where κ is the thermal conductivity, ρ is the density of the materials, c is the specific heat capacity, T is the temperature, and Q is the density of the heat source. Similarly, in the Lagrange coordinate system, the term v in Eq. (7) will be changed to implicit. The heat sources for railguns include Joule heat $Q_j = J^2/\sigma$ and frictional heat $Q_f = fv$, where f is friction. In the simulation, the static and dynamic friction coefficients are taken as 0.3 and 0.15, respectively.

The Joule heat consists of two parts, the first is heat generated by the metal resistance, the other is the Joule heat generated by the contact resistance. The heat generated by the contact resistance acts partially on the rails, and this ratio is expressed by the coefficient D_r:

$$D_r=\frac{\sqrt{\kappa_r\rho_r c_r}}{\sqrt{\kappa_r\rho_r c_r}+\sqrt{\kappa_a\rho_a c_a}}, \tag{8}$$

where the subscripts a and r correspond to the armature and rails, respectively. The ratio of contact resistance heat obtained by the armature is $D_a = 1 - D_r$.

The contact resistance was calculated according to the Contact Layer model (CLM model) [15]:

$$\rho_c l_c=\rho_a c\left(\frac{H_{soft}}{P}\right)^m, \tag{9}$$

where ρ_c is the contact resistivity, l_c is the thickness of the nominal contact layer, ρ_a is the arithmetic mean of the resistivities of the two contact materials, H_{soft} is the hardness of the armature, and P is the contact pressure. m and c are empirical contact constants measured experimentally, the values of m and c are related to material properties. For railguns, $m = 0.63$ and $c = 9.45 \times 10^{-4}$.

For simulation, the current shown in Fig. 3 is loaded into the breech end of the rails as a source term (in the form of average current density). Fixed constraint is applied to the outer surface of the rails and the armature is in contact with the rails. The ambient temperature is set to 273 K.

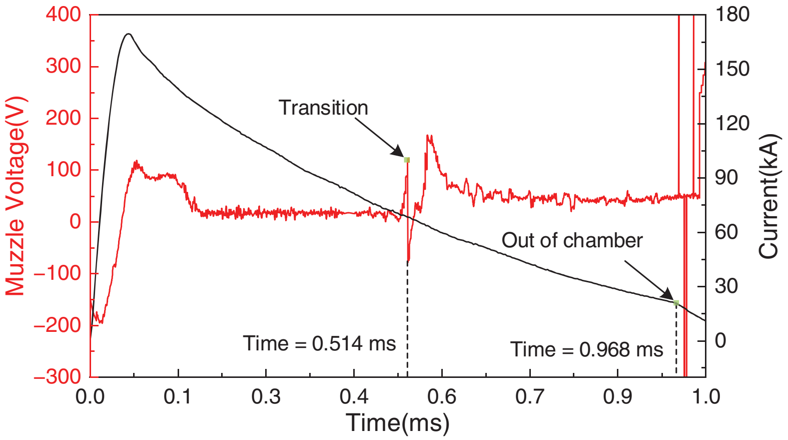

Figure 3: Muzzle voltage and current

3 Behavior of the Armature in the Chamber

3.1 *Test Results for Current, Muzzle Voltage and Armature Velocity*

Fig. 3 shows the current and muzzle voltage waveforms measured after the launch test used in this paper. It can be seen that the muzzle voltage rises sharply at 0.514 ms, indicating that an increase in resistance between the armature and rails occurs at this time, suggesting that an electrical breakdown (also known as a transition) occurs at this moment. It is important to note that the muzzle voltage is different from the electrode voltage: a sudden increase in muzzle voltage indicates a change in the contact state, but does not imply an increase in the electrode voltage. In addition, at 0.968 ms, a greater rate of decrease in pulse current can be seen, indicating that the armature is out of the chamber at this point. The pulsed current waveforms in Fig. 3 are also the currents used for the simulation. According to joint time-frequency analysis, at the rise edge of the current, the frequency of the current decreases rapidly from 3900 to 3200 Hz, and at the drop edge of the current, the frequency of the current is maintained at about 3200 Hz.

3.2 *Armature Preloading Simulation*

Reliable contact between the armature and rails is achieved by an interference fit. Due to the stiffness and shape of the armature, the trail end of the armature arm cannot be fitted to the rails, which is known as contact separation (called initial separation). Fig. 4 illustrates the distribution of contact pressure on the armature surface and armature deformation after assembly. It is clear that the contact pressure is concentrated in the throat of the armature and the deformation of the armature arm occurs mainly at the tail end of the armature arm.

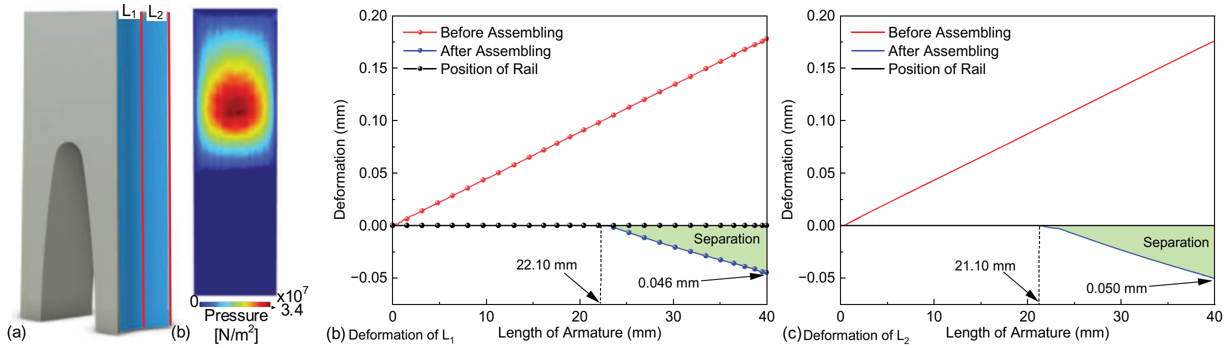

Figure 4: Armature loading results

Fig. 4b,c shows the deformation on the straight line L_1 and L_2 in Fig. 4a and it can be seen that the contact separation occurs in the latter part of the armature arm (after 21 mm), and the maximum separation reaches 0.05 mm, the deformation of L_2 is larger than that of L_1, and the phenomenon of contact separation occurs earlier in L_2 than in L_1.

3.3 *Armature Movement Simulation*

Once the armature is loaded (preloaded), it is powered through the pulse current shown in Fig. 3, and the armature advances under electromagnetic force. Fig. 5 shows the simulation curves of the armature kinematic characteristics and the armature. The time and velocity of the armature when it is out of the chamber, as measured by the light screen, are also labeled in Fig. 5 with blue color blocks.

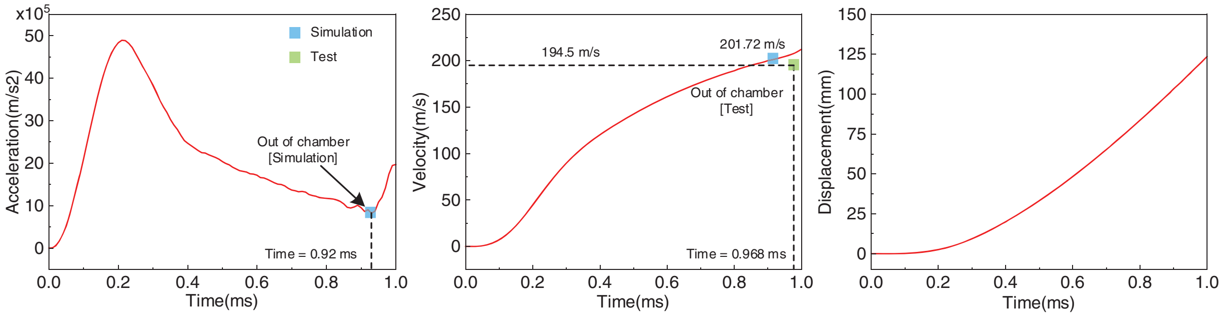

Figure 5: Current and armature motion parameters

The total simulation time is 1 ms and the current peaks at 167.23 kA at 0.23 ms. From Fig. 5a, it can be seen that the armature acceleration increases rapidly at the moment of 0.92 ms, at which time the armature is out of the chamber. The armature velocity (out of the chamber) obtained by simulation is 201.72 m/s and the armature velocity (out of the chamber) obtained by test is 194.5 m/s.

Fig. 6 illustrates the magnetic flux density and current flow lines near the armature/rail at 0.8 ms to explain how the negative electromagnetic leads to electromagnetic contact separation at the drop edge of the current. Notice that the magnetic field strength is greatest behind the armature (in the circuit I). As the current decreases, the magnetic flux in the circuit I decreases and, according to *Lezn Law*, induced current will be generated in circuit I in the opposite direction of the pulsed current. The current flow on the armature is plotted in Fig. 6b, where the flow lines of the induced and pulsed currents can be seen. It can be observed that the induced current interacting with the magnetic field will produce electromagnetic force F_{neg} in the opposite direction of the contact force F_{pos}. F_{neg} will change the force state of the armature, inducing the armature arm to separate from the rails. That is, based on the initial separation, the electromagnetic force F_{pos} first causes the armature arm to be fully affixed to the rails (full face contact). When the current reaches the drop edge, F_{neg} will separate the armature from the rails (electromagnetic separation) as the electromagnetic force decreases and the negative electromagnetic force appears.

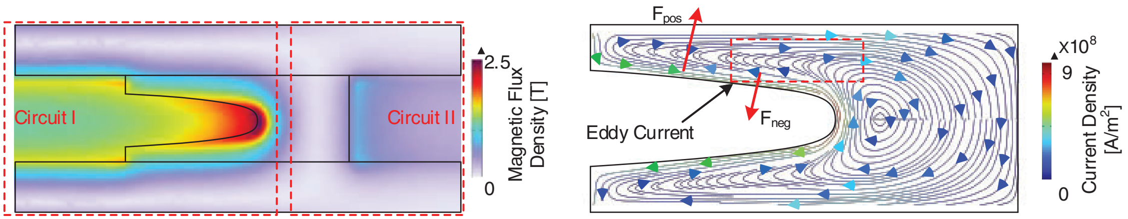

(a) Magnetic Flux Density Distribution (b) Current Density Flow Line

Figure 6: Magnetic density and current distribution at 0.8 ms

Further, we observe the distribution of x-direction electromagnetic forces (the coordinate system is shown in Fig. 1) on the armature as shown in Fig. 7. We showed only half of the armature to make observation more easily. It can be seen that at the rising stage of the current, there is almost no opposite electromagnetic force on the armature arm; at the drop stage of the current, the opposite electromagnetic force is mainly concentrated on the two sides of the tail of the armature arm. In addition, the armature head under the influence of eddy current also has a lower density of opposite electromagnetic force.

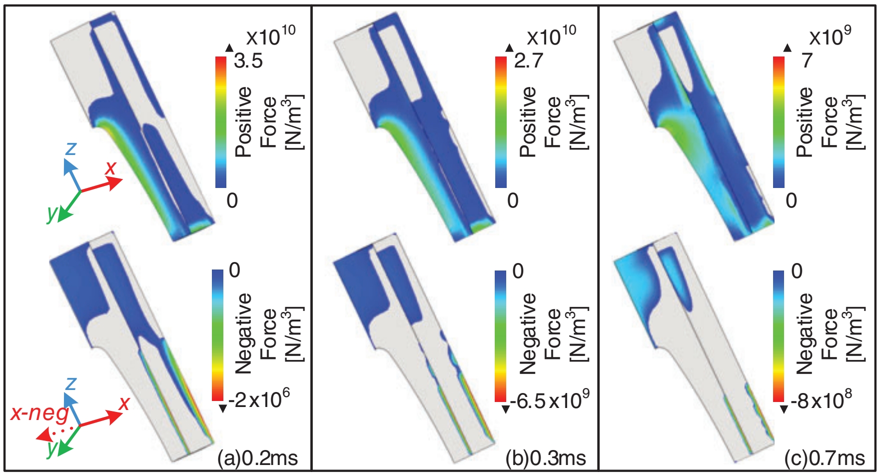

Figure 7: Distribution of Lorentz force in x-direction on the armature

In addition, we counted the change of contact force with time, as shown in Fig. 8, where F_c represents the contact force, F_t is the electromagnetic force in the z-direction whose effect is to thrust the armature forward, F_{np} and F_{nn} are the electromagnetic force in x-positive direction and in x-negative direction on half of the armature (the effect of F_{np} is to fit the armature arm to the rails and the effect of F_{nn} is to separate the armature arm from the rails). Notice that the contact force cannot be considered equal to F_{np} since we use elastic materials.

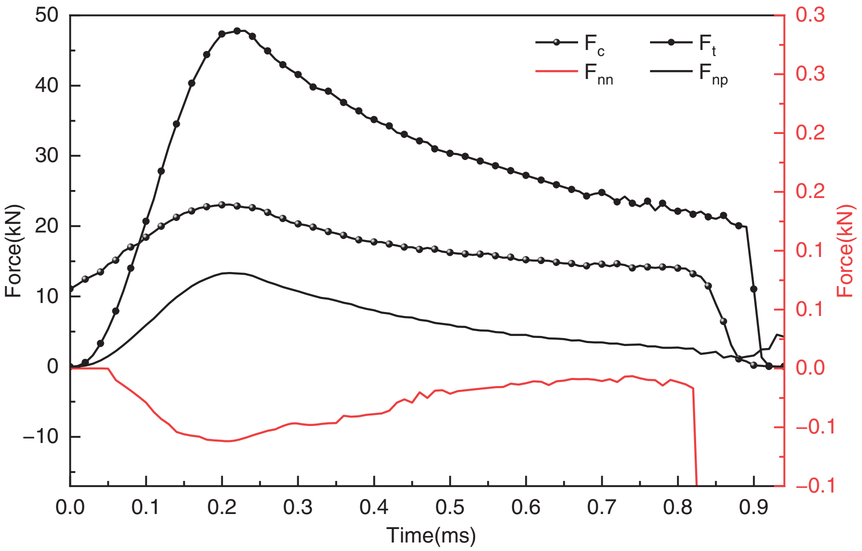

Figure 8: Force on the armature

It can be seen that the electromagnetic force follows essentially the same trend as the current. Although F_{nn} is much smaller than F_{np}, this force still causes contact separation due to the more concentrated distribution of F_{nn}. Corresponding to the change of armature acceleration, F_t decreases rapidly around 0.92 ms. While F_{nn}, F_{np}, and F_c decrease around 0.82 ms, which is due to the fact that at this time the armature starts to move out of the chamber, and the contact area between the armature and the rails decreases rapidly.

Fig. 9 shows the dynamic process of contact separation during armature movement in the chamber and Fig. 10 shows the statistics of parameters about contact separation, where $SepP_{\max}$ and $SepP_{\min}$ are the maximum and minimum values of the distance from the armature tail for the position at which the contact separation occurs, $PreP_{\max}$ is the distance from the armature tail for the position at which the maximum value of the contact pressure occurs, $Dis_{\max}$ and Dis_{aver} indicate the maximum and the average values of the separation, respectively.

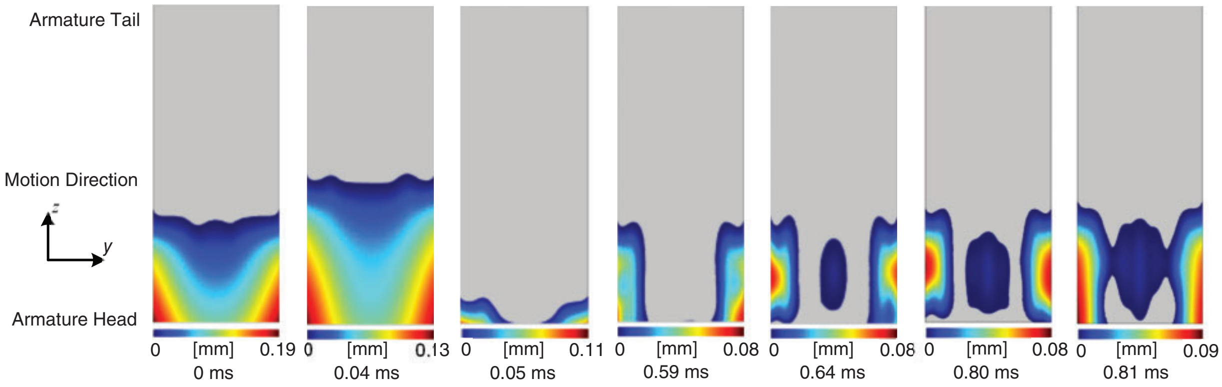

Figure 9: Contact separation during railgun operation

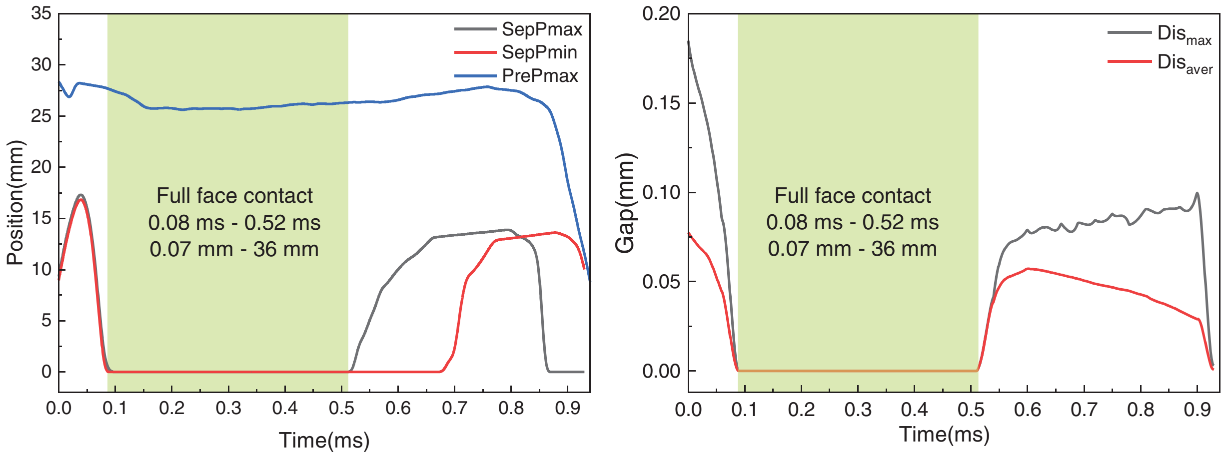

Figure 10: Parameters about contact separation

The area labeled green (from 0.08 to 0.52 ms) in Fig. 10 is the area where no contact separation occurs. It is noted that under the action of the interference fit, the armature appears to be in contact separation with the rails when the armature loading is completed; after energization, the armature is quickly and completely affixed to the rails under the action of the electromagnetic force, and the contact separation disappears (full face contact); After 0.52 ms, contact separation reappeared and remained until the armature left the rails. The following phenomenon deserves to be noted: (1) Despite the long full-face contact time (0.08–0.52 ms), the distance of armature movement at this stage is very short due to the slow velocity of the armature (0.07–36 mm); (2) Contact separation always occurs at the tail of the armature and decreases gradually from the tail to the head (along z-positive direction) and from the edge to the center (from $y \to \infty$ to $y = 0$). In addition, the length of the separation region (in the z-direction) remains essentially constant; (3) After energization, the magnitude of separation decreases dramatically; in the electromagnetic separation stage, the magnitude of separation is maintained at about half of the initial magnitude of separation. In fact, the area of the separation region is much smaller than the area of the initial separation region, despite the electromagnetic separation under F_{nn}.

3.4 Electrical and Thermal Properties on the Contact Surface

The armature-rail contact is an electrical contact with high temperatures and high loads, and the electrical and thermal characteristics are important contact parameters for railguns. Fig. 11 shows the temperature distribution on the armature at different times, and Fig. 12 shows the temperature distribution on the rails. Fig. 12a–c is the results on line (a), line (b) and line (c), respectively. The legend in Fig. 12b indicates the correspondence between curve color and time, and it holds true for Fig. 12a,c.

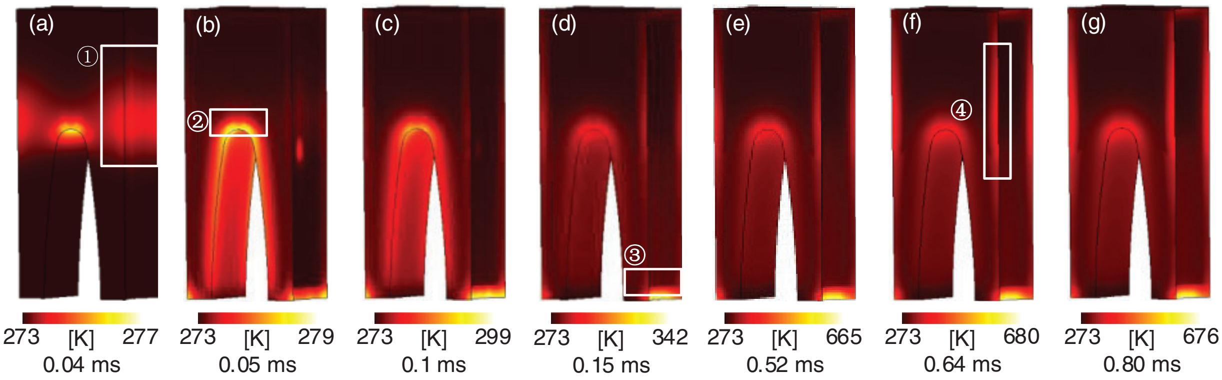

Figure 11: Temperature distribution on the armature

Obviously, the maximum temperature on the armature is much greater than that on the rails but doesn't exceed the melting point of 7075 aluminum alloy. In a general railgun, the armature almost always melts, but we use shorter rails and smaller currents to mitigate the melting (since the melting affects the size of the contact gap and is difficult to calculate accurately). On the armature, the temperature maximum occurs initially at the throat (as shown in Fig. 11b ②) and then shifts to the tail (as shown in Fig. 11d ③) of the armature. On the contact surface, a high-temperature region appeared in the middle section (as shown in Fig. 11a ①) of the contact surface at 0.04 ms; after 0.25 ms, the high-temperature region appeared on both sides of the middle section (as shown in Fig. 11f ④) of the contact surface. The tail of the armature remains high temperature throughout, but after 0.64 ms, the maximum temperature in this region decreases. The change of temperature distribution on the contact surface is affected by the contact separation: before 0.08 ms, the armature tail is in the contact separation state, and region ① has the highest contact pressure, so the frictional heat is the most; after 0.52 ms, the armature tail separates from the rails again, so the maximum temperature decreases.

Fig. 12 shows that the maximum temperature on the rails does not reach the melting point, indicating that the rails were not melted during launching. The location of the highest temperature on the rails always lags behind the armature, and the faster the armature the longer the lag. Notice that the temperature at the location on the rails in contact with the armature is always lower than the armature's temperature. This is because the current density on the armature is always greater than that on the rails. Considering the short operating time of the railgun, the armature and rails cannot reach thermal equilibrium, so we do not force the armature and rails temperatures to be equal.

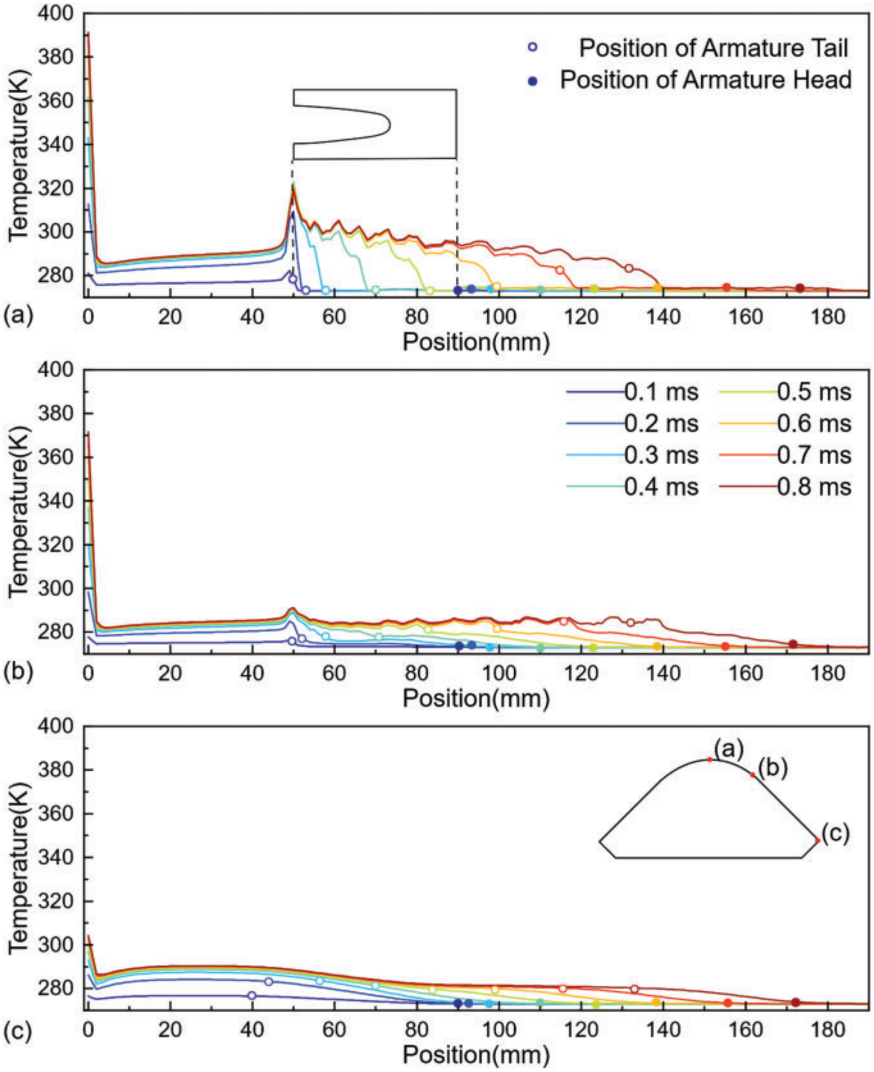

Figure 12: Temperature distribution on the rails

Fig. 13 shows the distribution of potential differences on the contact surface. The contact separation occurs only at the tail of the armature, and therefore the potential difference occurs only at the same place, and we have plotted only the tail of the armature 17.5 mm. It can be noticed that the distribution of the potential difference is very inhomogeneous and is always greater in the edge regions than in the center region. In the initial separation stage (before 0.08 ms), the maximum value of the potential difference increases with time. In the electromagnetic separation stage (after 0.52 ms), the maximum value of the potential difference increases slowly with time; the minimum value of the potential difference remains stable and close to 0 both in the initial separation and electromagnetic separation stages. Figs. 11 and 13 together illustrate that the maximum values of the potential difference and contact separation are more stable during the electromagnetic separation stage. Considering the small potential difference at the initial separation stage, we can determine that if electrical breakdown can be emitted, it will only occur at the electromagnetic separation stage and shortly after the start of electromagnetic separation. Moreover, once the electrical breakdown condition is satisfied, the electrical breakdown will continue.

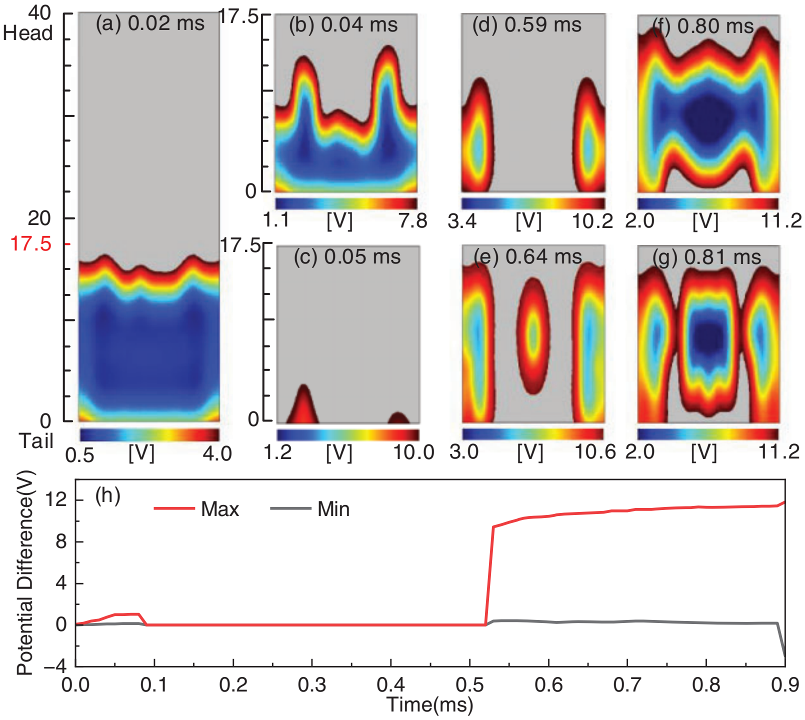

Figure 13: Potential difference distribution on the armature

4 Calculation of the Transition Moment

Railguns operate in an atmospheric environment and the gap formed by the contact separation is very small (not more than 1 mm), so we use the Townsend Discharge Model (improved by Rogowski) Eq. (10) to estimate the moment when the discharge between the armature and the rail occurs:

$$\gamma\left(\exp\left(\int_0^D N\alpha ds\right)-1\right), \tag{10}$$

where α and γ are the coefficients to describe the probability of collisional ionization occurring and the number of secondary electron emission. D is the distance of gaps, and s is the variables used in integration. When Eq. (10) is equal to 1, it means that the discharge condition is satisfied and when Eq. (10) is greater than 1, a self-maintained discharge occurs.

Fig. 3 shows the current and muzzle voltage waveforms measured after the launch test used in this paper. It can be seen that the muzzle voltage rises sharply at 0.514 ms, indicating that an increase in resistance between the armature and rails occurs at this time, suggesting that an electrical breakdown (also known as a transition) occurs at this moment. This time is earlier than the one obtained from the calculations in this paper (0.52 ms), which is due to the fact that the armature wear is not considered in the calculations in this paper.

It should be noted that in previous experiments, railguns with small caliber, low velocity, and small current (similar to the railgun used in this paper) usually did not cause transition. In this paper, an armature with a much smaller interference is used, and the contact force obtained is much lower (according to the "1g/A" law proposed by Marshall, a current of 160 kA requires at least 16 kN of contact force to be provided by the interference, and the initial contact force used in this railgun is 11 kN (as shown in Fig. 8)), which does not guarantee good armature-rail contact during operation, and thus the occurrence of a transition is predictable.

5 Conclusion

In this paper, the transition mechanism of the sliding electric contact pair is studied, and a transition judgment model based on the electric breakdown condition is proposed. Taking railguns as an example, the armature motion process is simulated by the FE/BE method, and the parameter changes during the contact between the armature and rails are analyzed. Results show that: (1) During the working of railguns, affected by the drop edge of the current, eddy currents are generated on the armature arm to cause the reversal of the contact force, which in turn leads to the phenomenon of contact separation between the armature and rails. (2) Under the potential difference between armature and rails, the air in the contact gap will be electrically broken, leading to the occurrence of transition, so that the railgun can't work properly.

Based on the above analysis, the following methods can be applied to suppress transition: (1) make railguns operate at the rising edge of current or flat-topped wave of current, which can be achieved by changing the parameters of the Pulse-forming Networks (PFN); (2) increase the amplitude of interference, which will lead to a greater contact force between the armature and rails; (3) fill the chamber of the railgun with gases with good electrical insulating properties, such as Sulfur hexafluoride (SF_6).

The limitation of this research is that the model used in this paper ignores the effects of wear and ablation on the separation gap, so the calculation results are somewhat different from the test. When faster railguns are used, wear is difficult to ignore, which is our future research goal.

Acknowledgement: Not applicable.

Funding Statement: The authors received no specific funding for this study.

Author Contributions: The authors confirm contribution to the paper as follows: Conceptualization, Xiangyu Du and Shaowei Liu; methodology, Xiangyu Du; software, Xiangyu Du; validation, Xiaoquan Lu and Tianyou Zheng; formal analysis, Tianyou Zheng; investigation, Xiangyu Du; resources, Shaowei Liu; data curation, Xiangyu Du and Xiaoquan Lu; writing, Xiangyu Du; writing—review and editing, Shaowei Liu and Bo Cao; visualization, Xiangyu Du; supervision, Shaowei Liu; project administration, Shaowei Liu. All authors reviewed the results and approved the final version of the manuscript.

Availability of Data and Materials: The data that support the findings of this study are available from the Corresponding Author, Shaowei Liu, upon reasonable request.

Ethics Approval: Not applicable.

Conflicts of Interest: The authors declare no conflicts of interest to report regarding the present study.

References

1. Chemerys VT. Key problems of railgun: new concept for their resolution. Procedia Eng. 2013;58:377–83. doi:10.1016/j.proeng.2013.05.043.
2. Shen J, Fan SB, Ji YX. Aerodynamics analysis of a hypersonic electromagnetic hun launched rrojectile. Def Technol. 2020;16(4):753–61.

3. Mao W, Pang T, Guo Z. Analysis of the research progress of electromagnetic railgun based on CiteSpace. IEEE Access. 2024;12:3499–513. doi:10.1109/access.2023.3349028.
4. Kuribayashi S, Onozuka M, Oda Y, Ogino M, Shimizu K, Tamura H, et al. Development of railgun system to pellet injection for fusion reactor refueling. In: Fusion technology. Amsterdam, The Netherlands: Elsevier; 1991. p. 660–4
5. Onozuka M, Oda Y, Kuribayashi S, Azuma K, Satake K, Kasai S, et al. Development of railgun system for high-speed pellet injection. In: Fusion technology. In, Amsterdam, The Netherlands: Elsevier; 1993. p. 599–603.
6. Barber JP, Bauer DP, Jamison KA. A survey of armature transition mechanisms. IEEE Trans Magn. 2003;39(1):47–51. doi:10.1109/tmag.2002.805913.
7. Cong H, Zhou Y, Zhaori G, Wang Y, Wei H, Liu Z, et al. Principle issues and future prospect on sliding arc ablation of metal rail. J Electr Eng Technol. 2024;19(3):1685–700. doi:10.1007/s42835-023-01598-6.
8. Guo A, Du X, Wang X. Calculation of armature melting wear rate based on contact surface heat distribution. IEEE Trans Plasma Sci. 2024;52(7):1011–20. doi:10.1109/tps.2024.3406713.
9. Wang Z, Chen L, Ren Y, Xu J, You P, Lan X, et al. Muzzle voltage of conventional and augmented railguns. IEEE Trans Plasma Sci. 2022;50(10):3802–8. doi:10.1109/tps.2022.3205338.
10. Mcglasson BT, Small MT, Catterlin JK. Commissioning experiments at the naval postgraduate school pulsed power and EM launch laboratory. IEEE Trans Plasma Sci. 2022;50(10):3311–7. doi:10.1109/tps.2022.3180978.
11. Zhu CY, Li BM. Analysis of sliding electric contact characteristics in augmented railgun based on the combination of contact resistance and sliding friction coefficient. Def Technol. 2020;16(4):747–52. doi:10.1016/j.dt.2019.12.007.
12. Dong E, Cao R, Hao X. Research on the inner bore profile detecting system of railgun. Measurement. 2020;150:107053. doi:10.1016/j.measurement.2019.107053.
13. Gendel YG, Glushkov IS, Kareev YA. Dynamics of armature acceleration in a railgun channel. Tech Phys Lett. 2013;39(4):397–409. doi:10.1134/s1063785013040172.
14. Machado BI, Murr LE, Martinze E. Materials characterization of railgun erosion phenomena. Mater Sci Eng A. 2011;528(25):7552–9.
15. Hsieh KT, Satapathy S, Hsieh MT. Effects of pressure-dependent contact resistivity on contact interfacial conditions. IEEE Trans Magn. 2009;45(1):313–8. doi:10.1109/tmag.2008.2008876.